Static compression of Fe4N to 77 GPa and its implications for nitrogen in the deep Earth

REVISION 1

Static compression of Fe_4N to 77 GPa and its implications for nitrogen in the deep Earth

Helene Breton[1], Tetsuya Komabayashi[1], Samuel Thompson[1], Nicola Potts[1], Chris McGuire[1], Sho Suehiro[2], Simone Anzellini[3], and Yasuo Ohishi[4]

[1]School of GeoSciences and Centre for Science at Extreme Conditions, University of Edinburgh EH9 3FE, UK

[2]Department of Earth and Planetary Sciences, Tokyo Institute of Technology, Tokyo 152-8551, Japan

[3]Diamond Light Source Ltd., Diamond House, Science & Innovation Campus, Didcot, OX11 0DE, UK.UK

[4]SPring-8, Japan Synchrotron Radiation Research Institute, 1-1-1 Kouto, Sayo-cho, Sayo-gun, Hyogo 679-5198, Japan

*corresponding author: Helene Breton

E-mail: H.Breton@ed.ac.uk

ABSTRACT

Compression and decompression experiments on face-centred cubic (fcc) γ′-Fe_4N to 77 GPa at room temperature were conducted in a diamond anvil cell with *in-situ* X-ray diffraction (XRD) in order to examine its stability under high pressure. In the investigated pressure range, γ′-Fe_4N did not show any structural transitions. However, a peak broadening was observed in the XRD pattern above 60 GPa. The obtained pressure-volume data to 60 GPa were fitted to the third-order Birch-Murnaghan equation of state (EoS), which yielded the following elastic parameters: K_0 = 169 (6) GPa, K' = 4.1 (4), with a fixed V_0 = 54.95 Å at 1 bar. A quantitative Schreinemakers' web was obtained at 15-60 GPa and 300-1600 K by combining the EoS for γ′-Fe_4N with reported phase stability data at low pressures. The web indicates the existence of an invariant point at 41 GPa and 1000 K where γ′-Fe_4N, hexagonal closed-packed (hcp) ε-Fe_7N_3, double hexagonal closed-packed β-Fe_7N_3, and hcp Fe phases are stable. From the invariant point, a reaction γ′-Fe_4N = β-Fe_7N_3 + hcp Fe originates towards the high pressure side, which determines the high-pressure stability of γ′-Fe_4N at 56 GPa and 300 K. Therefore, the γ′-Fe_4N phase observed in the experiments beyond this pressure must be metastable. The obtained results support the existing idea that β-Fe_7N_3 would be the most nitrogen-rich iron compound under core conditions. An iron carbonitride $Fe_7(C,N)_3$ found as a mantle-derived diamond inclusion implies that β-Fe_7N_3 and Fe_7C_3 may form a continuous solid solution in the mantle deeper than 1000 km depth. Diamond formation may be related to the presence of fluids in the mantle and dehydration reactions of high-pressure hydrous phase D might have supplied free fluids in the mantle at depths greater than 1000 km. As such, the existence of $Fe_7(C,N)_3$ can be an indicator of water transportation to the deep mantle.

Key words

Iron nitrides, Earth's core, equation of state, diamond anvil cell, in situ X-ray diffraction, high-pressure

INTRODUCTION

Knowledge of the distribution of volatile elements within the solid Earth is a key to understanding the origin and evolution of the Earth as well as those of terrestrial atmosphere. One of the potential volatile storage sites in the deep Earth is considered to be the core, which is linked to one of the major issues with the core, namely, light element in the core. The comparison of geophysical observations and laboratory experiments shows that the Earth's core is likely less dense than pure iron (or an iron-nickel alloy) (Birch 1952). The value for the so-called core density deficit (cdd) has been revised based on high-pressure experimental measurement of iron density and recent estimates range from 3.6 to 4.6 % for the solid inner core at 6000 K (Dewaele et al., 2006; Fei et al., 2016). The cdd has often been associated with the presence of light element(s) including O, S, H, C, and Si (Poirier 1994). The identification of the kind and amount of the light elements in the core places constraints on the origin, formation, and evolution of the Earth because redistribution of light elements into an iron-rich core should depend on a number of thermodynamic conditions during core formation.

As a major volatile element in the atmosphere, the presence of water/hydrogen in the core and its consequences have been discussed (e.g., Okuchi 1998; Nomura et al. 2014) as well as its circulation in the mantle (e.g., Komabayashi 2006). On the other hand, nitrogen which is another major component of the atmosphere has received less attention and its circulation and storage in the deep Earth were less studied (Mikhail et al. 2017; Minobe et al. 2015; Litasov et al. 2017; Bajgain et al. 2018) despite of its abundance in meteorite from

thousand ppm (chondrites) to 1 wt% (iron meteorites) (see Litasov et al. (2017) and reference therein). In order to discuss the storage of nitrogen in the core, phase relations in the system Fe-N should first be elucidated.

Another potential storage site for nitrogen is the mantle. Mantle-derived diamonds are contaminated by nitrogen up to 1500 ppm (Cartigny 2005). Various mineral inclusions were found in those diamonds and their parageneses may indicate high pressure conditions of formation in the deep mantle (Kaminsky and Wirth 2011). Minobe et al. (2015) discussed that one of the inclusions, $Fe_7(C,N)_3$ phase, may indicate that its origin would be deeper than 1000 km based on the stability of Fe_7N_3 phases. On the other hand, diamond formation may be related to the presence of C-H-N-O fluids in the mantle (Harte 2010). As such analyzing the stability of iron nitride phases may enable us to place constraints on the presence of fluid in the deep mantle.

Phase relations of the system Fe-N at 1 bar (e.g., Göhring et al. 2016) show that the Fe-rich solid compounds in the system, which could be candidates for the inner core structure, include γ′-Fe_4N and ε-Fe_3N_x with x = 0.75-1.4 (Leineweber et al. 1999; Niewa et al. 2009; Widenmeyer et al. 2014). The γ′-Fe_4N phase has a cubic perovskite structure with a face-centered cubic (fcc) arrangement of Fe atoms along with a single N atom placed at the centre of the structure (Jacobs et al. 1995). ε-Fe_3N_x has a hexagonal closed-packed (hcp) structure similar to ε-Fe with N atoms occupying the octahedral interstices of the layered Fe atoms (Jacobs et al. 1995). In contrast to γ′-Fe_4N, the crystallographic configuration of hcp ε-Fe_3N_x allows a wide range of N stoichiometry ranging between ε-Fe_3N and ε-$Fe_3N_{1.5}$ (~ ε-Fe_7N_3) (Leineweber et al. 1999; Widenmeyer et al. 2014) with x changing as a function of temperature (Litasov et al. 2013).

High-pressure-temperature (*P-T*) stability of ε-Fe_3N_x was studied by Minobe et al. (2015) who examined phase relations of Fe_7N_3 (i.e., x~1.3 in Fe_3N_x) in a laser-heated diamond anvil cell (DAC). They showed that ε-Fe_7N_3 was transformed into double hexagonal closed-packed β-Fe_7N_3 at 40 GPa and 1000 K which is stable at least to 150 GPa and 2720 K. On the other hand, the stability of γ′-Fe_4N was examined to 30 GPa in multianvil apparatus. It transforms to ε-Fe_3N_x at 1373 K and 8.5 GPa (x = 0.75, Guo et al. 2013), 1600 K and 15 GPa (x = 0.95, Niewa et al. 2009), and at 1273 K and 30.5 GPa (x = 0.80, Litasov et al. 2013). The stability of γ′-Fe_4N was poorly constrained above 30 GPa. Minobe et al. (2015) used γ′-Fe_4N as a starting material and collected its XRD pattern at 99 GPa and 300 K. Then they conducted laser heating on the sample and the following reaction took place,

$$3\ \gamma'\text{-}Fe_4N = \beta\text{-}Fe_7N_3 + 5\ \varepsilon\text{-Fe} \quad \text{.....(1)}$$

The temperature of reaction (1) was not well constrained as it was below the minimum temperature measurable by the spectroradiometric method (ca. 1300 K), but they considered 1000 ± 300 K (Minobe et al. 2015). As such, the stability of γ′-Fe_4N under high pressures may not be tightly constrained by the laser-heated DAC technique. In addition, Adler and Williams (2005) argued that the transition in γ′-Fe_4N might be kinetically impeded as they observed gradual weakening of the diffraction peaks with increasing pressure. If reaction (1) observed in Minobe et al. (2015) was due to the metastable existence of γ′-Fe_4N to 99 GPa, the possibility that it might not be an equilibrium univariant reaction remains. One potential approach to the thermodynamic stability of γ′-Fe_4N under high pressure is to construct a Schreinemakers' web using existing phase equilibrium data under low pressure and predict the possible location of reaction (1). Since Fe_4N is the most iron-rich compound in the system Fe-N, whether reaction (1) is an equilibrium univariant reaction or not, and if it exists, its *P-T*

location should be constrained for the discussion about the constituent phase of the inner core.

Here we conducted static compression and decompression experiments of γ′-Fe_4N to 77 GPa with *in-situ* X-day diffraction (XRD) to examine its stability at 300 K. From the collected pressure-volume (*P-V*) data, we evaluated its equation of state (EoS) and the dP/dT slope of reaction (1) from the Clausius-Clapeyron relation. The elastic properties of γ′-Fe_4N were only studied to 32 GPa (Adler and Williams 2005), while those of β-Fe_7N_3 were to 132 GPa (Minobe et al. 2015). We constructed a quantitative Schreinemakers' web for the phase relations involving Fe_4N, Fe_7N_3, and Fe and discuss the thermodynamic stability of γ′-Fe_4N and its implications for Earth's core and the origin of carbonitrides found in diamond inclusions.

EXPERIMENTAL PROCEDURE

Compression experiments were performed in a DAC. High pressures were generated with a pair of diamond anvils with a 300 μm culet. Rhenium gaskets were pre-indented to a thickness of 30 μm before a hole with a diameter of 100 μm was drilled to form a sample chamber. The starting material was powdered Fe_4N (Kojundo Chemical Lab. Co. Ltd.). The commercially available powder contained a slight amount of pure Fe. An XRD measurement at 1 bar and 300 K on the starting material was employed at the University of Edinburgh. Rietveld refinement on the XRD pattern revealed the sample is a mixture of 91 % γ′-Fe_4N and 9 % Fe. The sample was sandwiched between 10-μm-thick layers of KCl, which served as pressure transmitting medium and pressure marker (Dewaele et al. 2012). To remove air

moisture, the DAC was dried in a vacuum oven at 383 K for 8 hours prior to pressurization at room temperature.

In-situ XRD experiments were conducted at beamline I15 (Anzellini et al. 2018) at the Diamond Light Source synchrotron facility, UK, using monochromatic X-rays with a wavelength of 0.4246 Å. The X-ray beam size at the sample position was 9 μm x 6 μm (full-width at half maximum, FWHM). The XRD data collected on a 2-D detector (Perkin Elmer) was integrated into one-dimensional pattern with the Fit2d program (Hammersley et al. 1996). Another series of compression experiments were made at beamline BL10XU, SPring-8 (Ohishi et al., 2008). Monochromatic incident X-rays were focused and collimated to an area of 6-μm (FWHM) at the sample position with a wavelength of 0.4146 Å. A 2-D flat panel detector (Perkin Elmer XRD 0822) collected the XRD data. At both beamlines, the typical exposure time was 1 second. In all the runs, pressures were calculated from the unit-cell volume of the internal pressure calibrant KCl according to the EoS proposed by Dewaele et al. (2012).

RESULTS

Compression behaviour of γ′-Fe_4N

Four separate sets of compression/decompression experiments of γ′-Fe_4N were performed between 22 and 77 GPa at 300 K. A representative XRD pattern of the sample is shown in Figure 1. The unit-cell volume of γ′-Fe_4N was obtained based on the (111) diffraction line as the (200) diffraction peak was not always present in the diffraction patterns. The experimental conditions are summarized in Table 1.

The runs 1-3 were conducted at I15 and the run 4 was at BL10XU. In the first run, we started collecting XRD patterns at 38 GPa and compressed the sample to 72 GPa. Then a decompression cycle was performed to 39 GPa. The *P-V* data in both compression and decompression cycles overlap (Fig. 2). In the second and third runs, the samples were directly compressed to 33 and 75 GPa respectively. In the fourth run, a one-way compression run was conducted from 22 to 77 GPa. Figure 2 plots results from this study and Adler and Williams (2005). When one compares different datasets, the consistency between pressure scales used in each study needs to be critically evaluated. Adler and Williams (2005) used ruby as a pressure calibrant while we used KCl. We recalculated the pressure values in Adler and Williams (2005) based on the lattice constant of Au embedded in their sample chamber, using the pressure scale by Sokolova et al. (2016). The pressure scales set by Sokolova et al. (2016) is consistent with the EoS of KCl by Dewaele et al. (2012) which is used as the pressure marker in this study. As such the plots in Figure 2 are based on the consistent pressure scales. Our results are consistent with Adler and Williams (2005) at 20-30 GPa where the data overlap.

In all the runs, to the highest pressure of 77 GPa, γ′-Fe_4N sustained its structure without a pressure-induced phase transformation, which reproduced the results of Minobe et al. (2015) who observed γ′-Fe_4N to 99 GPa at 300 K. In order to closely examine the effect of pressure on the structure of γ′-Fe_4N, we plotted the FWHM of the peak (111) as a function of pressure (Fig. 3). The FWHM of γ′-Fe_4N was normalised to that of KCl as the peak width is sensitive to the stress state in the sample chamber (Komabayashi et al., 2007). While the error bars of several data points are fairly large, a peak broadening is clearly observed above 60 GPa, suggesting that the structure of γ′-Fe_4N might not be stable under those pressures.

The isothermal compression and decompression data were fitted to the third-order Birch-Murnaghan (BM) EoS:

$$P = \frac{3K_0}{2}\left[\left(\frac{V_0}{V}\right)^{7/3} - \left(\frac{V_0}{V}\right)^{5/3}\right]\left\{1 - \frac{3}{4}(4 - K')\left[\left(\frac{V_0}{V}\right)^{2/3} - 1\right]\right\} \quad \text{.....(2)}$$

where V_0, K_0, and K' are the unit-cell volume, isothermal bulk modulus, and its pressure derivative at 1 bar and 300 K. We considered only the data up to 60 GPa as the data collected at greater pressures showed the peak broadening as mentioned above. We also adopted the data by Adler and Williams (2005) since their data coverage was complementary to ours at higher pressures (Fig. 2). A least squares fit yields K_0 = 169 (6) GPa and K' = 4.10 (4) with a fixed V_0 = 54.95 Å (Adler and Williams 2005). The resulting compression curve is illustrated in Figure 2.

The normalized volume, V/V_0, of γ′-Fe_4N as a function of pressure is plotted in Fig. 4 together with existing data (ε-Fe_7N_3, Adler and Williams 2005; β-Fe_7N_3, Minobe et al. 2015). For comparison, other iron-alloys systems are also shown (ε-Fe-9wt%Si, Tateno et al. 2015; ε-Fe_7C_3, Nakajima et al. 2011; γ-Fe, Komabayashi 2014; ε-Fe, Fei et al. 2016). The hcp structure (ε) of Fe becomes less compressible with the addition of Si, C, or N. In contrast, the fcc structure (γ) increases its compressibility when nitrogen is added to iron, which is similar to the case of hydrogen (Narygina et al. 2011). Note that γ′-Fe_4N does not form a solid solution with γ-Fe at 1 bar (Göhring et al. 2016) as it occurs only as a stoichiometric compound (Jacobs et al. 1995) and therefore, the comparison made here is exclusively qualitative.

Subsolidus phase relations of the system Fe-N

185 The present experiments did not observe any decomposition/transformation of γ′-
186 Fe_4N to 77 GPa although a peak broadening for the sample was seen above 60 GPa. Minobe
187 et al. (2015) showed that the structure was immediately decomposed upon laser heating at 99
188 GPa. They reported the temperature for the reaction was 1000 ± 300 K. The large uncertainty
189 came from the difficulty in measuring low temperature by the spectroradiometric method and
190 implies that constraining its *P-T* location in a laser heating experiment is difficult. The phase
191 equilibria of γ′-Fe_4N were therefore assessed from the construction of a Schreinemakers' web
192 at 20-60 GPa in the system Fe-N. An invariant point in a binary system consists of four
193 phases from the Gibbs phase rule. Existing experiments reported γ′-Fe_4N, ε-Fe_7N_3, β-Fe_7N_3,
194 ε-Fe, and γ-Fe in this pressure range (Niewa et al. 2009; Komabayashi et al. 2009; Litasov et
195 al. 2013; Minobe et al. 2015). Since five phases are present, at least two invariant points need
196 to be recognised. From the reported experimental data, we identified the following invariant
197 points: (i) ε-Fe, γ-Fe, ε-Fe_7N_3, and γ′-Fe_4N; (ii) ε-Fe, β-Fe_7N_3, ε-Fe_7N_3, and γ′-Fe_4N (Fig. 5).
198 Then a web of reactions was constructed; three univariant reactions originate from each
199 invariant point. The *P-T* locations of reactions were then constrained by experimental phase
200 equilibrium data (Niewa et al. 2009; Komabayashi et al. 2009; Litasov et al. 2013; Minobe et
201 al. 2015). Results show that invariant point (i) is located at 29 GPa and 1310 K and invariant
202 point (ii) is at 41 GPa and 1000 K. All the reactions originating from each invariant point are
203 listed in Table 2. Reaction (1) γ′-Fe_4N = ε-Fe + β-Fe_7N_3 that determines the stability of γ′-
204 Fe_4N originates from invariant point (ii) towards the high pressure side.

205 In order to predict the *P-T* location of reaction (1), the Clausius-Clapeyron relation for
206 each reaction in the constructed Schreinemakers' web was assessed. The Clausius-Clapeyron
207 equation is expressed as:

208 $$\frac{dP}{dT} = \frac{\Delta S}{\Delta V} \quad \text{.....(3)}$$

where ΔS and ΔV are the change in entropy and volume of the reaction respectively. For ε-Fe-N alloys, (i.e., Fe_3N_x) we assumed the same x of 1.3 (i.e., Fe_7N_3) for the *P-T* condition studied.

The following reactions from invariant point (i) were first assessed:

$$\gamma'\text{-}Fe_4N = \gamma\text{-}Fe + \varepsilon\text{-}Fe_7N_3 \quad \text{.....(4)}$$

$$\gamma\text{-}Fe = \varepsilon\text{-}Fe \quad \text{.....(5)}$$

$$\gamma'\text{-}Fe_4N = \varepsilon\text{-}Fe + \varepsilon\text{-}Fe_7N_3 \quad \text{.....(6)}$$

The values for ΔS, ΔV and slope for reaction (5) were provided by Komabayashi (2014). The *P-T* locations and slopes for reactions 4 and 6 were each constrained by one experimental data point; ΔV were calculated at 300 K using the EoS constructed above for γ′-Fe_4N together with the EoS of Alder and Williams (2005) for ε-Fe_7N_3. Then we optimised their dP/dT values and ΔS simultaneously so that the calculations reproduce the experimental data (Fig. 5). For invariant point (ii), we assumed the same ΔS, ΔV and dP/dT slope for reaction (6). The slope and ΔV for the reaction:

$$\varepsilon\text{-}Fe_7N_3 = \beta\text{-}Fe_7N_3 \quad \text{.....(7)}$$

were given in Minobe et al. (2015) and ΔS was evaluated in this study. Then ΔS for reaction (1) was obtained through reactions (6) and (7) and the dP/dT value was calculated from equation (3). The optimised parameters set for all the reactions is given in Table 2 and the calculated boundaries are shown in Figure 5.

Figure 5 illustrates that the reactions involving γ′-Fe_4N have negative dP/dT slopes, which indicates that the entropy differences are positive. Table 2 shows that those reactions are indeed characterised by large positive entropy differences, which is caused by a larger

231 entropy of Fe_7N_3 compared to γ′-Fe_4N. This would be due to the different dissolution
232 mechanisms of nitrogen in the structures. As mentioned earlier, nitrogen goes into interstitial
233 sites in ε-Fe_3N_x structure and therefore the configurational entropy should be larger than for
234 γ′-Fe_4N where nitrogen substitutes for iron. A recent computational study revealed the
235 structure of β-Fe_7N_3 which is characterised by the absence of a close-packed arrangement of
236 iron unlike ε-Fe_3N_x and γ′-Fe_4N (Gavryushkin et al., 2018). This may also explain the high
237 entropy of β-Fe_7N_3.

238 Recently Gavryushkin et al. (2018) predicted a new form of Fe_7N_3 which take an
239 orthorhombic structure with the space group of *Amm2*. *Amm2*-Fe_7N_3 may be stable between
240 ε-Fe_7N_3 and β-Fe_7N_3 at 0K. They suggested that the *Amm2* phase might not be stable at high
241 temperature, which should be clarified in the near future.

242 Figure 5 shows that reaction (1) originating from the invariant point (ii) is located at
243 56 GPa at 300 K. This indicates that γ′-Fe_4N observed at higher pressures in this study and
244 Minobe et al. (2015) should be metastable. Indeed, we observed a peak broadening in the
245 XRD pattern for γ′-Fe_4N at pressures higher than 60 GPa (Fig. 3). Therefore, the
246 instantaneous decomposition of γ′-Fe_4N upon laser heating at 99 GPa observed in Minobe et
247 al. (2015) was due to the metastable presence of the phase at 300 K and their reported
248 temperature of 1000 ± 300 K for its decomposition is for the kinetic boundary.

249

250 **IMPLICATIONS**

251 In the present study, the high-pressure stability of γ′-Fe_4N was defined by reaction (1)
252 which takes place at 56 GPa and 300 K. Here we extend the discussion further to very high
253 pressures, examining the relative stability of each side of reaction (1) under core pressures
254 based on the volume, which expresses the pressure dependence of the Gibbs free energy. A

255 similar argument was made earlier by Adler and Williams (2005) with ε-Fe_7N_3 instead of β-
256 Fe_7N_3 on reaction (1) because the high-pressure form, β-Fe_7N_3 was not known at that time
257 (Minobe et al. 2015). Figure 6 shows the molar volume of each side of reaction (1) as a
258 function of pressure to 400 GPa based on the latest EoS for each phase (γ′-Fe_4N, this study;
259 Fe, Fei et al. (2016); β-Fe_7N_3, Minobe et al. (2015)). The assemblage of β-Fe_7N_3 + 5 ε-Fe
260 shows a smaller volume than 3 γ′-Fe_4N at all the pressures, similar to the case in Adler and
261 Williams (2005) with ε-Fe_7N_3. This means that once the assemblage of β-Fe_7N_3 + 5 ε-Fe has
262 been stabilised, γ′-Fe_4N will never be stabilised with increasing pressure. As such, γ′-Fe_4N
263 cannot be a candidate for Earth's inner core. As Minobe et al. (2015) suggested, therefore, the
264 likely stable nitride in Earth's inner core would be β-Fe_7N_3, although the presence of a further
265 phase transition of β-Fe_7N_3 above 150 GPa and 2720 K cannot be ruled out.

266 Minobe et al. (2015) and Litasov et al. (2017) argued that the nitrogen content in the
267 inner core to account for a 10% cdd assuming a mixture of hcp Fe + β-Fe_7N_3 would be 9.5
268 wt%. Minobe et al. (2015) however discussed that the maximum nitrogen content in the core
269 should be about 1 wt% from its abundance in CI chondrites. From the first principles
270 calculations of the sound velocity and density of the Fe-N liquids, Bajgain et al. (2018)
271 concluded that the nitrogen content in the outer core would be less than 2 wt%. As such, the
272 estimated nitrogen content in the core is not high and there must be some other light elements
273 in there. Due to the low nitrogen content in the core, β-Fe_7N_3 could only be formed if the
274 eutectic composition is very Fe-rich and direct measurements of the melting phase relation of
275 the system Fe-N under inner conditions should be studied in the future.

276 Whether β-Fe_7N_3 would sink or float in the outer core is another important issue when
277 it is precipitated from the liquid outer core. Minobe et al. (2015) reported that the
278 compression behaviours and molar volumes of β-Fe_7N_3 and Fe_7C_3 are very similar to core

279 pressures. Hence we here assume the same thermal parameters for β-Fe_7N_3 as for Fe_7C_3
280 (Nakajima et al., 2011). The calculated density of β-Fe_7N_3 at 5000 K and 330 GPa is 12.47
281 g/cm^3, which is denser than the outer core (12.17 g/cm^3) and less dense than the inner core
282 (12.76 g/cm^3). As such it should sink in the outer core although Fe_7N_3 alone cannot meet the
283 inner core density.

284 The stability of nitrides under high-*P*-*T* conditions can place constraints on the origin
285 of mantle-derived diamonds. Here we make a case study of mineral inclusions found in
286 diamonds from Juina, Brazil (Kaminsky and Wirth 2011). From mineral parageneses of the
287 inclusions, Kaminsky and Wirth (2011) suggested that the origin of these diamonds might be
288 in the deep Earth. The list of mineral inclusions they found included an $Fe_7(C,N)_3$ phase with
289 N/N+C = 0.27. From its nitrogen:carbon ratio, Minobe et al. (2015) argued the possibility of
290 the formation of a continuous solid solution between β-Fe_7N_3 and Fe_7C_3 as they have the
291 same or very similar structures (Nakajima et al 2011; Minobe et al. 2015). If this is the case,
292 the stability of β-Fe_7N_3 indicates a deep mantle origin. On the other hand, diamond formation
293 may be related to the presence of fluids in the mantle and dehydration reactions in subducting
294 slabs in the mantle should be important (Harte 2010). There are expected major dehydration
295 zones along the subduction of a slab: ~300 km (10 GPa) depth and ~700 km depth (25 GPa)
296 (Komabayashi 2006). Those depths are however, in the stability field of ε-Fe_7N_3 which would
297 not form a solid solution with Fe_7C_3. High-pressure hydrous phase D may be a water carrier
298 into the deep lower mantle (Komabayashi 2006). Dehydration reactions of phase D is
299 expected to occur at depths greater than 1000 km (40 GPa) if the slab temperature is lower
300 than 1300 K (Nishi et al. 2014), which is in the stability field of β-Fe_7N_3. As such the
301 presence of the $Fe_7(C,N)_3$ phase in diamonds may indicate the water transportation to the
302 deep lower mantle.

ACKNOWLEDGEMENTS

Synchrotron XRD measurements were carried out at beamlines BLI15 at the Diamond Light Source (ref number: ee17683-1) and BL10XU at the SPring-8 (ref number: 2018B1464). We thank K. Litasov and an anonymous reviewer for their helpful comments on the manuscript. This work is supported by the Natural Environment Research Council (NERC) (No. NE/M000346/1) and by the European Research Council (ERC) Consolidator Grant to T.K. (No. 647723).

312 **References**

313

314 Adler, J.F., and Williams, Q. (2005) A high-pressure X-ray diffraction study of iron nitrides:
315 Implications for Earth's core. Journal of Geophysical Research, 110, 1-11.

316 Anzellini, S., Kleppe, A.K., Daisenberger, D., Wharmby, M.T., Giampaoli, R., Broccato, S.,
317 Baron, M.A., Miozzi, F., Keeble, D.S., Ross, A., Gurney, S., Thompson, J., Knap, G.,
318 Booth, M., Hudson, L., Hawkins, D., Walter, M.J., Wilhelm, H. (2018) Laser-heating
319 system for high-pressure X-ray diffraction at the extreme conditions beamline I15 at
320 Diamond Light Source. Journal of Synchrotron radiation, 25, 1860-1868.

321 Bajgain, S., Mookherjee, M., Dasgupta, R., Gosh, D.B., and Karki, B.B. (2018) Nitrogen
322 content in the Earth's outer. Geophysical Research Letter, 46, 89-98.

323 Birch, F. (1952) Elasticity and constitution of the Earth's interior. Journal of Geophysical
324 Research, 57, 227-286.

325 Cartigny, P. (2005) Stable isotopes and the origin of diamond. Elements, 1(2), 79–84.

326 Dewaele, A., Loubeyre, P., Occelli, F., Mezouar, M., Dorogokupets P.I., and Torrent M.
327 (2006) Quasihydrostatic equation of state of iron above 2Mbar. Physical Review
328 Letters, 97, 215504.

329 Dewaele, A., Belonoshko, A.B., Garbarino, G., Occelli, F., Bouvier, P., Hanfland, M., and
330 Mezouar, M. (2012) High-pressure–high-temperature equation of state of KCl and
331 KBr. Physical Review B, 85, 214105.

Fei, Y., Murphy, C., Shibazaki, Y., Shahar, A., and Huang, H. (2016) Thermal equation of state of hcp-iron: Constraint on the density deficit of Earth's solid inner core. Geophysical Research Letters, 43, 6837-6843.

Gavryushkin P.N., Sagatov N.E., Popov Z.I., Bekhtenova A.E., Inerbaev T.M., Litasov K.D. (2018) Structure and properties of new high-pressure phase of Fe7N3. JETP Letters, 107(6), 379-383.

Göhring, H., Fabrichnaya, O., Leineweber, A., and Mittemeijer, E.J. (2016) Thermodynamics of the Fe-N and Fe-N-C systems: the Fe-N and Fe-N-C phase diagrams revisited. Metallurgical and materials transactions A, 47 A, 6173-6186.

Guo, K., Rau, D., Von Appen, J., Prots Y., Schnelle, W., Dronkowski, R., Niewa, R., and Schwarz, U. (2013) High pressure high-temperature behavior and magnetic properties of Fe4N: experiment and theory. High Pressure Research, 33, 684-696.

Hammersley, A.P. (1996) FIT2D: a multi-purpose data reduction, analysis and visualization program. Journal of Applied Crystallography, 49, 646-652.

Harte, B. (2010) Diamond formation in the deep mantle: the record of mineral inclusions and their distribution in relation to mantle dehydration zones. Mineralogical Magazine, 74, 189-215.

Jacobs, H., Rechenbach, D., and Zachwieja, U. (1995) Structure determination of γ′-Fe4N and ϵ-Fe3N. Journal of Alloys and Compounds, 227, 10-17.

Kaminsky, F., and Wirth, R. (2011) Iron carbide inclusions in lower-mantle diamond from Juina, Brazil, The Canadian Mineralogist, 49, 555-572.

353 Komabayashi, T. (2006) Phase relations of hydrous peridotite: implications for water
354 circulation in the Earth's mantle. In AGU monograph 168 *Earth's Deep Water Cycle*
355 (eds: S. Jacobsen and S. van der Lee), AGU, 29-43.

356 Komabayashi, T., Hirose, K., Sata, N., Ohishi, Y., and Dubronsky, L.S. (2007) Phase
357 transition in $CaSiO_3$ perovskite. Earth and Planetary Science Letters, 260, 564-569.

358 Komabayashi, T., Fei, Y., Meng, Y., and Prakapenka, V. (2009) In-situ X-ray diffraction
359 measurements of the γ-ε transition boundary of iron in an internally-heated diamond
360 anvil cell. Earth and Planetary Science Letters, 282, 252-257.

361 Komabayashi, T. (2014) Thermodynamics of melting relations in the system Fe-FeO at high
362 pressure: Implication for oxygen in the Earth's core. Journal of Geophysical
363 Research, 119, 4164-4177.

364 Leineweber, A., Jacobs, H., Hüning, F., Lueken, H., Schilder, H., and Kockelmann, W.
365 (1999) ε-Fe3N: magnetic structure, magnetization and temperature dependent disorder
366 of nitrogen. Journal of Alloys and Compounds, 288, 79-87.

367 Litasov, K.D., Shatskiy, A.F., Ovchinnikov, S.G., Popov, Z.I., Ponomarev, D.S., and Ohtani,
368 E. (2013) Phase Transformations of Fe3N–Fe4N Iron Nitrides at Pressures up to 30
369 GPa Studied by In Situ X-ray Diffractometry. JETP Letters, 98, 805-808.

370 Litasov, K.D., Shatskiy, A.F., Ponomarev, D.S., and Gavryushkin, P.N. (2017) Equations of
371 state of iron nitrides ε-Fe3Nx and γ-Fe4Ny to 30 GPa and 1200 K and implication for
372 nitrogen in the Earth's core. Journal of Geophysical Research: Solid Earth, 122, 3574-
373 3584.

374 Marty, B., Avice, G., Sano, Y., Altwegg, K., Balsiger, H., Hassig, M., Morbidelli, A.,
375 Mousis, O., and Rubin, M. (2016) Origins of volatile elements (H, C, N, noble gases)

on Earth and Mars in light of recent results from the ROSETTA cometary mission. Earth and Planetary Science Letters, 441, 91-102.

Mikhail, S., Barry, P.H., and Sverjensky, D.A. (2017) The relationship between mantle pH and the deep nitrogen cycle. Geochimica et Cosmochimica Acta, 209, 149-160.

Minobe, S., Nakajima, Y., Hirose, K., and Ohishi, Y. (2015) Stability and compressibility of a new iron-nitride β-Fe7N3 to core pressures. Geophysical Research Letters, 42, 5206-5211

Nakajima, Y., Takahashi, E., Sata, N., Nishihara, Y., Hirose, K., Funakoshi, k.-I., and Ohishi, Y. (2011) Thermoelastic property and high-pressure stability of Fe7C3: Implication for iron-carbide in the Earth's core. American Mineralogist, 96, 1158–1165.

Niewa, R., Rau, D., Wosylus, A., Meier, K., Wessel, M., Hanfland, M., Dronskowski, R., Schwarz, U. (2009) High-pressure high-temperature phase transition of γ′-Fe4N. Journal of Alloys and Compounds, 480, 76-80.

Nishi, M., Irifune, T., Tsuchiya, J., Tange, Y., Nishihara, Y., Fujino, K., Higo, Y. (2014) Stability of hydrous silicate at high pressures and water transport to the deep lower mantle. Nature Geoscience, doi:10.1038/NGEO2074.

Nomura, R., Hirose, K., Uesugi, K., Ohishi, Y., Tsuchiyama, A., Miyake, A., Ueno, Y. (2014) Low Core-Mantle Boundary Temperature Inferred from the Solidus of Pyrolite. Science, 343, 522-525.

Ohishi, Y., Hirao, N., Sata, N., Hirose, K., and Takata, M. (2008) Highly intense monochromatic X-ray diffraction facility for high-pressure research at spring-8. High Pressure Research, 28, 163-173.

Okuchi, T. (1997) Hydrogen partitioning into molten iron at high pressure: Implications for Earth's core. Science, 278, 1781-1784.

Poirier, J.-P. (1994) Light elements in the Earth's outer core: A critical review. Physics of the Earth and Planetary Interiors, 85, 319-337.

Sokolova T.S, Dorogokupets P.I., Dymshits A.M., Danilov B.S., Litasov K.D., Microsoft excel spreadsheets for calculation of PVT relations and thermodynamic properties from equations of state of MgO, diamond and nine metals as pressure markers in high-pressure and high-temperature experiments. Computers and Geosciences, 94, 162-169.

Tateno, S., Kuwayama, Y., Hirose, K., and Ohishi, Y. (2015) The structure of Fe–Si alloy in Earth's inner core. Earth and Planetary Science Letters, 418, 11-19.

Widenmeyer, M., Hansen, T.C., Meissner, E., and Niewa, R. (2014) Formation and Decomposition of Iron Nitrides Observed by in situ Powder Neutron Diffraction and Thermal Analysis. Journal of Inorganic and General Chemistry, 640, 1265-1274.

420 **Figure captions**

421 Figure 1. Representative XRD pattern of γ′-Fe_4N together with Fe (initially present in the
422 starting material) and KCl at 75 GPa and 300 K.

423

424 Figure 2. Unit-cell volume of γ′-Fe_4N as a function of pressure at 300 K. The solid and
425 dashed lines are calculated compression curves from EoS based on a combination of our data
426 and those of Adler and Williams (2005) and the result of Adler and Williams (2005)
427 respectively. Only the compression data of Adler and Williams (2005) were used. For
428 comparison, a compression curve for γ-Fe at 300 K (Komabayashi 2014) is shown. The data
429 taken up to 60 GPa were used for the fitting to the EoS of γ′-Fe_4N.

430

431 Figure 3. Full width at half maximum (FWHM) of the dominant (111) peak of γ′-Fe_4N
432 normalized to that of the (110) peak of KCl. Above 60 GPa, a peak broadening was observed.
433 The grey line is a guide to the eye.

434

435 Figure 4. Compression curves of iron nitrides, iron and other iron alloys (γ′-Fe_4N, this study;
436 ε-Fe, Fei et al. (2016); ε-Fe_7C_3, Nakajima et al. (2011); ε-Fe_7N_3, Adler and Williams (2005);
437 β-Fe_7N_3, Minobe et al. (2015); ε-Fe-9wt%Si, Tateno et al. (2015)).

438

439 Figure 5. Schreinemakers' web for phase relations of the Fe-rich side of the Fe-N system.
440 The squares are experimental constraints on reactions (Niewa et al. 2009; Litasov et al. 2013).
441 Two invariant points are recognised: (i) at 29 GPa and 1310 K involving ε-Fe, γ-Fe, γ′-Fe_4N
442 and ε-Fe_7N_3 and (ii) at 41 GPa and 1000 K involving ε-Fe, γ′-Fe_4N, ε-Fe_7N_3 and β-Fe_7N_3.

443 The high-pressure stability of γ′-Fe_4N is determined by the reaction of γ′-Fe_4N = β-Fe_7N_3 + ε-
444 Fe at 56 GPa and 300 K (the coefficients are omitted for clarity). The uncertainty range of the
445 reaction is due to the uncertainty in the EoS fitting.

446

447 Figure 6. Molar volumes of 3 γ′-Fe_4N and its isochemical assemblage of β-Fe_7N_3 + 5 ε-Fe as
448 a function of pressure. The volume of the assemblage of β-Fe_7N_3 + 5 ε-Fe (red) is smaller
449 than that of 3 γ′-Fe_4N (blue) implying that once transformed, γ′-Fe_4N will not be stabilised
450 anymore upon further compression.

451

452
453
454
455
456
457
458
459
460
461
462
463
464
465
466
467
468
469

Table 1. Experimental conditions and unit-cell volume of γ′-Fe_4N

Run	Beam line	Compression/ Decompression[2]	*a* of KCl (Å)	*P* (GPa)	*V* of γ′-Fe_4N (Å^3)
#1	I15	C	3.182	38.32	47.05
		C	3.179	39.74	46.74
		C	3.132	46.98	45.82
		C	3.107	52.22	44.85
		C	3.078	58.49	44.42
		C	3.059	63.01	43.87
		C	3.031	70.55	43.04
		C	3.025	72.07	42.73
		D	3.032	70.25	43.11
		D	3.088	56.32	44.22
		D	3.085	57.03	44.38
		D	3.109	51.79	44.70
		D	3.148	44.13	45.61
		D	3.178	38.96	46.28
#2	I15	C	3.216	33.13	47.48
#3	I15	C	3.014	75.22	42.16
#4	BL10XU	C	3.305	22.32	49.46
		C	3.305	22.35	49.45
		C	3.305	22.35	49.42
		C	3.234	30.62	48.38
		C	3.234	30.66	48.20
		C	3.187	37.48	46.84
		C	3.148	44.13	46.01
		C	3.115	50.43	44.95
		C	3.087	56.47	44.06
		C	3.066	61.43	43.20
		C	3.050	65.36	42.81
		C	3.029	70.96	41.88
		C	3.020	73.63	41.61
		C	3.007	77.39	40.82

[1]C, compression; D, decompression

Table 2. Clausius-Clapeyron equation for chemical reactions

Reaction	dP/dT, GPa/K	ΔV, cm^3/mol	ΔS, J/K/mol
Invariant point at 29 GPa and 1310 K			
3 γ′-Fe_4N = ε-Fe_7N_3 + 5 γ-Fe	- 0.0486	- 3.123	151.86
γ-Fe = ε-Fe[1]	0.0394	-0.0679	-2.67
3 γ′-Fe_4N = ε-Fe_7N_3 + 5 ε-Fe	- 0.0399	- 3.462	138.51
Invariant point at 41 GPa and 1000 K			
3 γ′-Fe_4N = ε-Fe_7N_3 + 5 ε-Fe	- 0.0399	- 3.462	138.51
ε-Fe_7N_3 = β-Fe_7N_3[2]	0.0029	- 2.670	- 7.628
3 γ′-Fe_4N = β-Fe_7N_3 + 5 ε-Fe	- 0.0213	- 6.132	130.88

[1] All the parameters are from Komabayashi (2014).

[2] The dP/dT slope and volume for β-Fe_7N_3 are from Minobe et al. (2015).

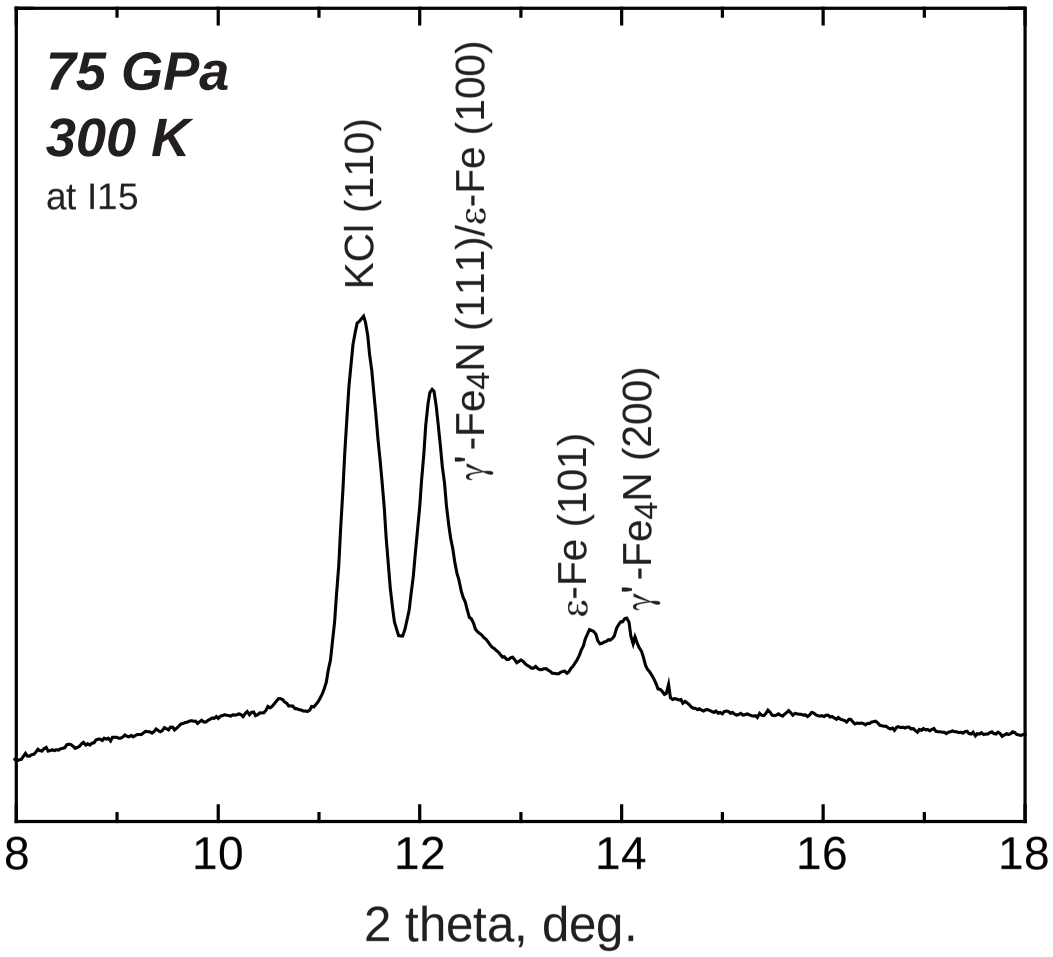
75 GPa
300 K
at I15
KCl (110)
γ'-Fe4N (111)/ε-Fe (100)
ε-Fe (101)
γ'-Fe4N (200)
8
10
12
14
16
18
2 theta, deg.

Figure 1

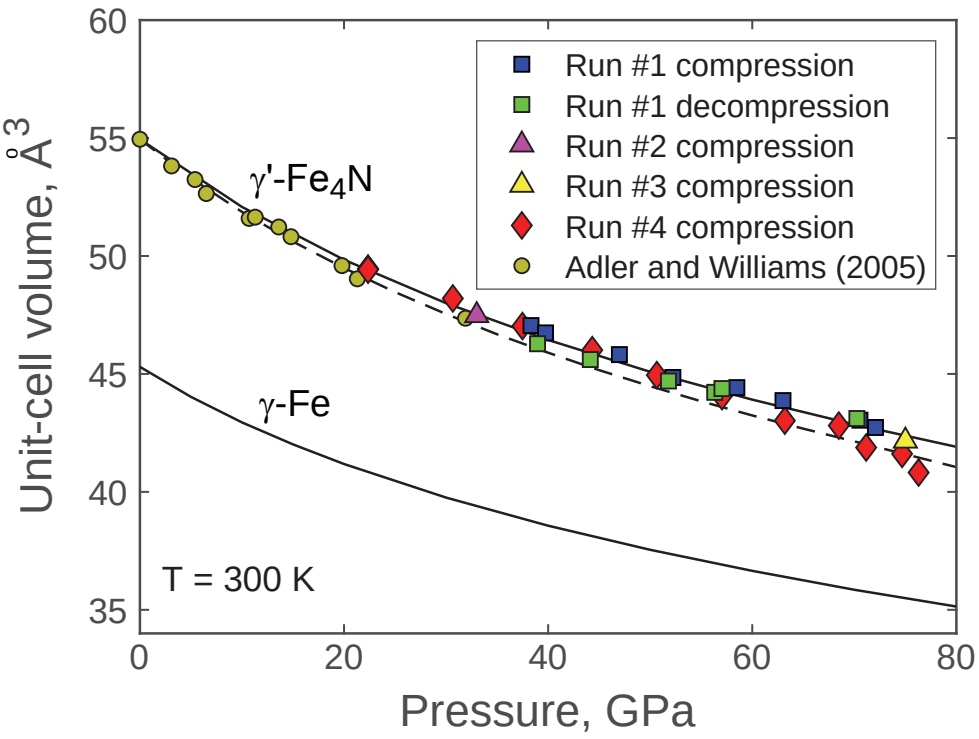
Unit-cell volume, Å3
Pressure, GPa
Run #1 compression
Run #1 decompression
Run #2 compression
Run #3 compression
Run #4 compression
Adler and Williams (2005)
γ'-Fe4N
γ-Fe
T = 300 K
60
55
50
45
40
35
0
20
40
60
80

Figure 2

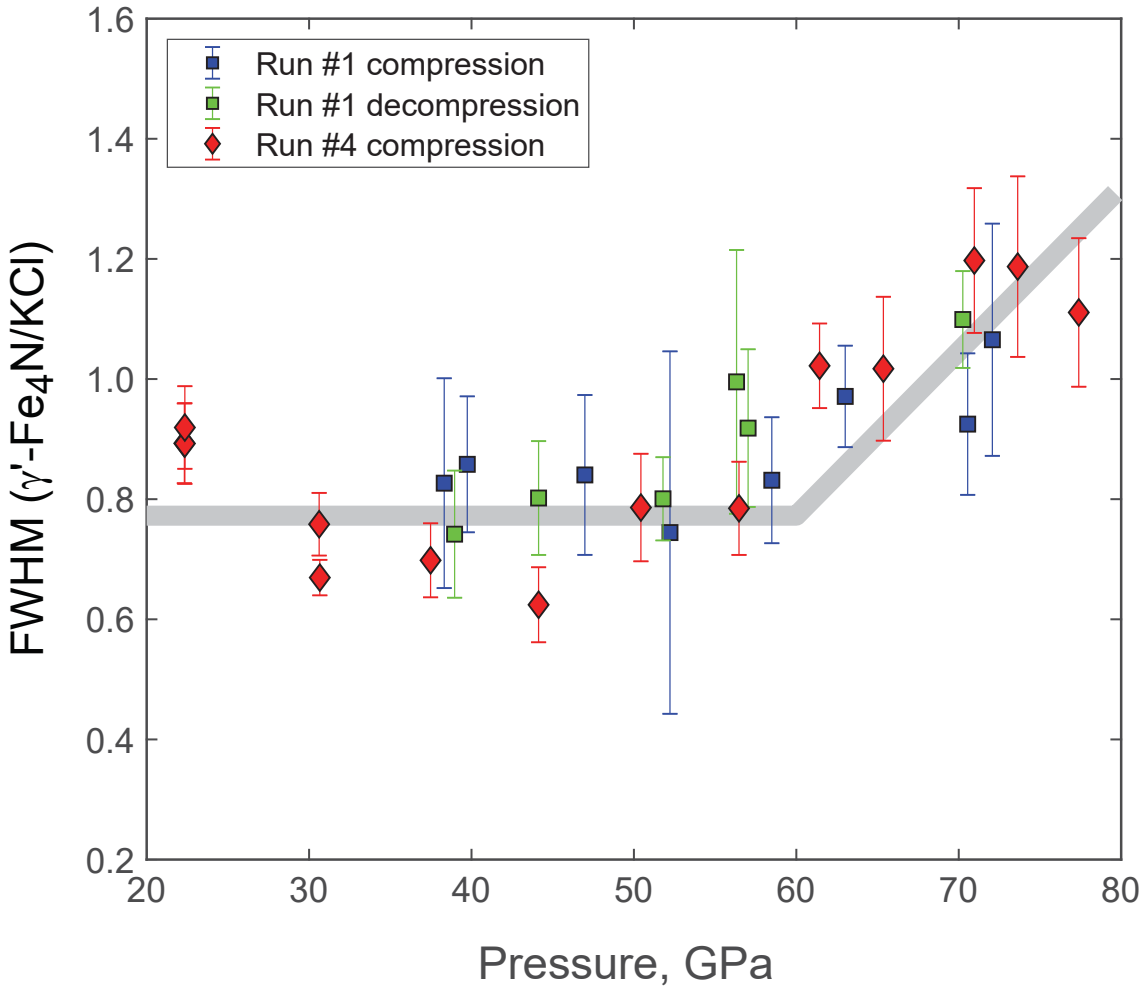
Run #1 compression
Run #1 decompression
Run #4 compression
FWHM (γ'-Fe4N/KCl)
Pressure, GPa
1.6
1.4
1.2
1.0
0.8
0.6
0.4
0.2
20
30
40
50
60
70
80

Figure 3

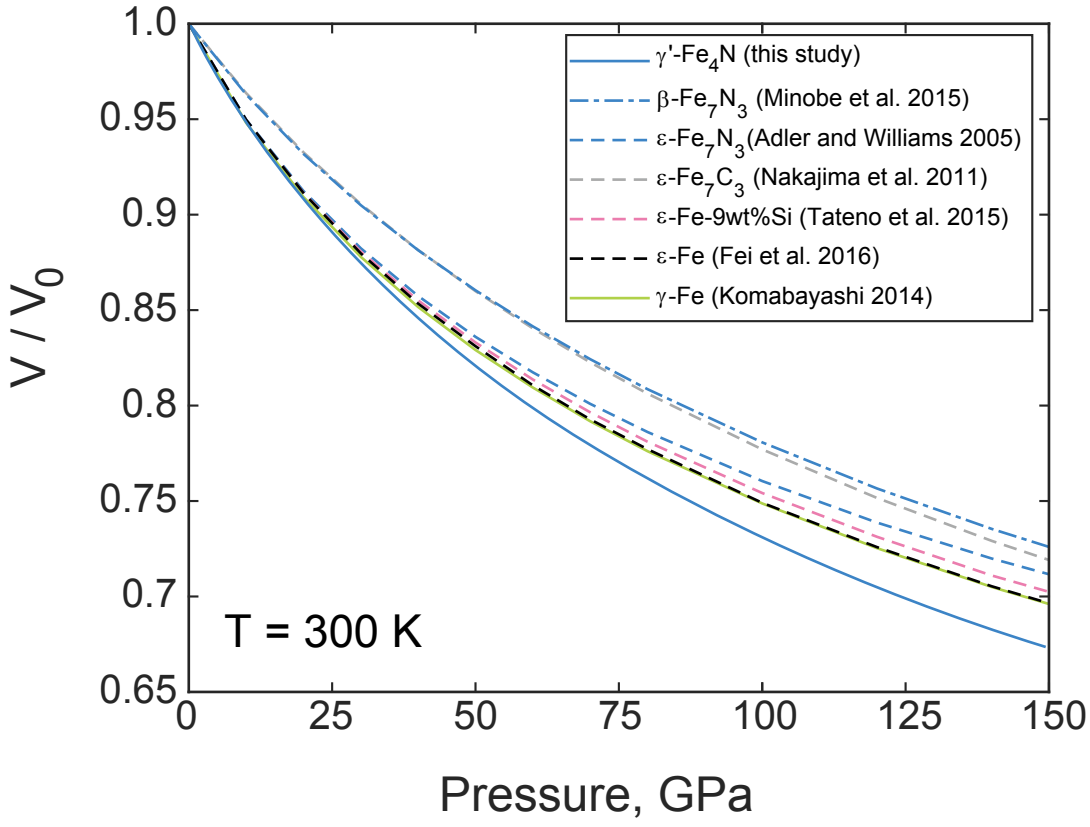
1.0
0.95
0.9
0.85
0.8
0.75
0.7
0.65
V / V0
0
25
50
75
100
125
150
Pressure, GPa
T = 300 K
γ'-Fe4N (this study)
β-Fe7N3 (Minobe et al. 2015)
ε-Fe7N3(Adler and Williams 2005)
ε-Fe7C3 (Nakajima et al. 2011)
ε-Fe-9wt%Si (Tateno et al. 2015)
ε-Fe (Fei et al. 2016)
γ-Fe (Komabayashi 2014)

Figure 4

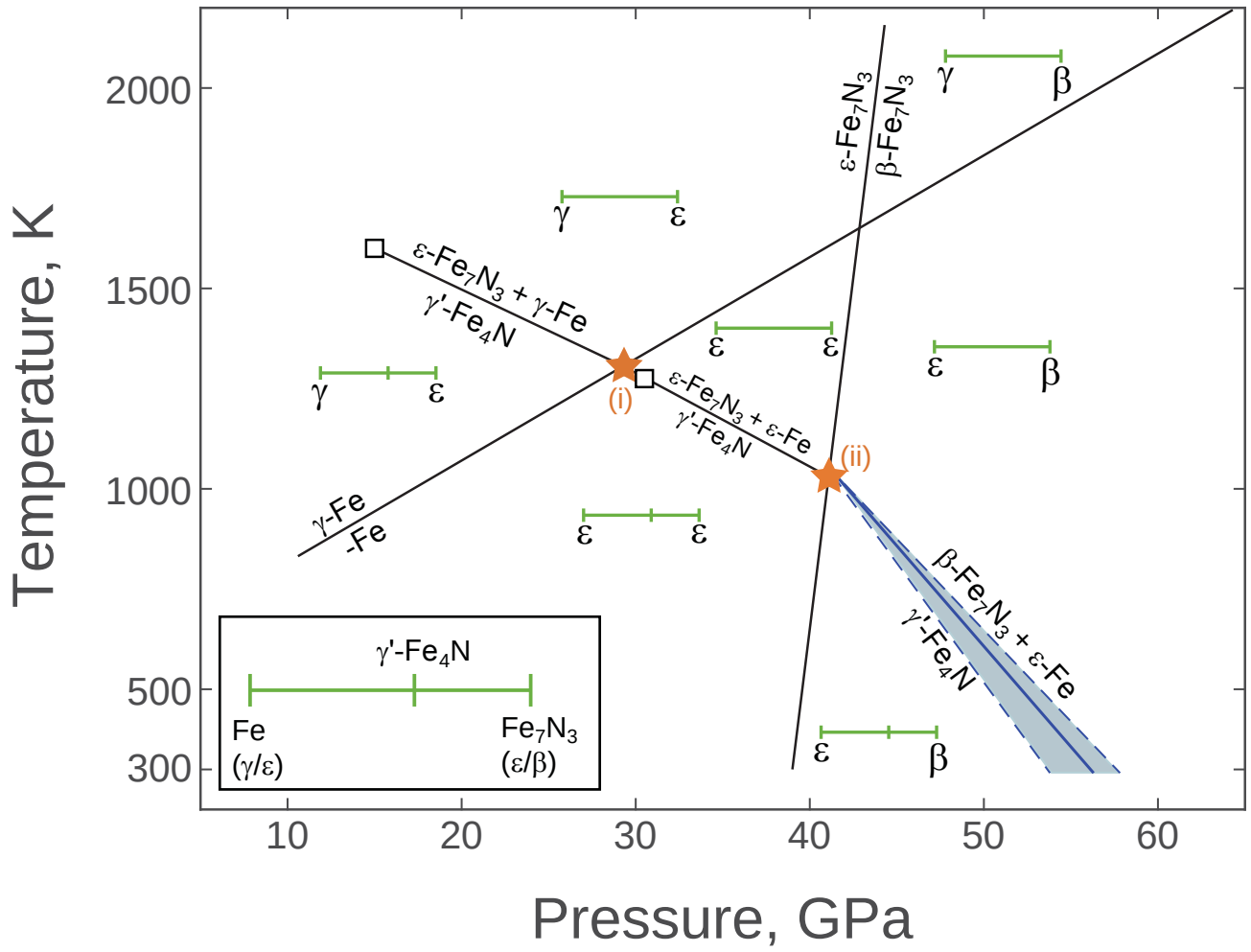
Temperature, K
2000
1500
1000
500
300
10
20
30
40
50
60
Pressure, GPa
γ
ε
β
ε-Fe7N3 + γ-Fe
γ'-Fe4N
ε-Fe7N3 + ε-Fe
γ'-Fe4N
γ-Fe
-Fe
ε-Fe7N3
β-Fe7N3
(i)
(ii)
β-Fe7N3 + ε-Fe
γ'-Fe4N
γ'-Fe4N
Fe
(γ/ε)
Fe7N3
(ε/β)

Figure 5

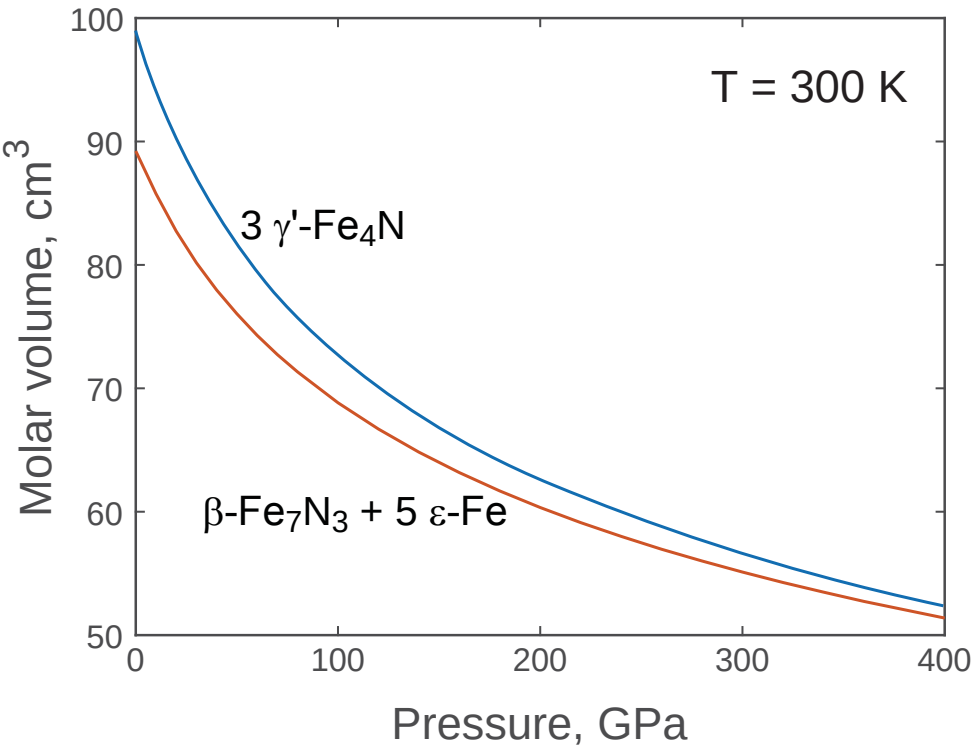
T = 300 K
3 γ'-Fe4N
β-Fe7N3 + 5 ε-Fe
Molar volume, cm3
Pressure, GPa
100
90
80
70
60
50
0
100
200
300
400

Figure 6